Gravitational and tectonic forces controlling postcollisional deformation and the present-day stress field of the Alps: Constraints from numerical modeling

I. Jiménez-Munt,[1,2] D. Garcia-Castellanos,[2,3] A. M. Negredo,[4] and J. P. Platt[1,5]

[1] We perform numerical modeling to investigate the mechanisms leading to the postcollisional tectonic evolution of the Alps. We model the lithospheric deformation as a viscous thin sheet with vertically averaged rheology and coupled with surface mass transport. The applied kinematic boundary conditions simulate the convergence between the Adria indenter and the European foreland during the last 35 Myr. Model predictions of elevation, lithospheric structure, erosion/sedimentation pattern and vertical axis rotation are compared with observations of the planform shape of the chain, topography, crustal thickness, distribution of rock exhumation and sediment thickness, and paleomagnetic rotations. Thickening of the lithosphere in the Alpine region is shown to be highly sensitive to the assumed viscosity law, to the strength contrasts between the different regions and to the surface mass transport. Modeling results indicate that the large-scale deformation of the Alps during the postcollisional phase is mainly controlled by accommodation of convergence in a weak orogenic zone caught between a nearly rigid Adria plate and a strong European foreland. Modeling of the present-day stress field shows that (1) the present rotation of Adria is responsible for the change of extension direction from strike-perpendicular in the western Alps to strike-parallel in the east and (2) the strike-perpendicular extension observed in the western Alps is likely due to lateral variations of gravitational potential energy. The results suggest a NNE shift of about 700 km of the Euler pole of Adria relative to Europe from its mean position during postcollisional deformation to the present day. **Citation:** Jiménez-Munt, I., D. Garcia-Castellanos, A. M. Negredo, and J. P. Platt (2005), Gravitational and tectonic forces controlling postcollisional deformation and the present-day stress field of the Alps: Constraints from numerical modeling, *Tectonics*, *24*, TC5009, doi:10.1029/2004TC001754.

1. Introduction

[2] The Alpine orogen is a classic example of a continent-continent collision zone, generally interpreted as a result of Africa-Eurasia convergence (Figure 1). The crustal and lithospheric structure, thermal evolution, and history of erosion and sedimentation in peripheral basins are all relatively well constrained, which makes the Alps a tempting target for geodynamic modeling of the collisional process. However, several outstanding questions, such as the role of Adria in Alpine collision, remain uncertain and can usefully be addressed by numerical modeling.

[3] The relative motion between Africa and Eurasia is relatively well constrained [*Dewey et al.*, 1989], with predominantly northward motion of Africa during the Tertiary. Adria is commonly treated as a promontory of Africa [e.g., *Channell et al.*, 1979], but this results in an overlap of Adria and Iberia in early Mesozoic reconstructions [*Wortmann et al.*, 2001]. *Platt et al.* [1989], however, used kinematic data from the Alps to suggest a predominantly WNW relative motion of Adria relative to Europe during the Neogene and possibly also the Paleogene, although the uncertainties with this approach increase going back in time. Because of these uncertainties in the motion history of Adria, the amounts of convergence at various stages of Alpine evolution are also uncertain. Roughly 1000 km of convergence between Africa and Adria has been accommodated in total since the mid-Cretaceous [*Dewey et al.*, 1989], but much of this is likely to have been taken up by subduction prior to collision. Estimates of postcollisional shortening based on restorations of structural sections across the Alps have been presented by *Platt* [1986] and *Menard et al.* [1991], and their results are used to simulate the postcollisional motion history in this study.

[4] The timing of collision in the Alps is also a matter of debate. Continental crust was first involved in contractional tectonics in the Alps in Late Cretaceous time [*Froitzheim et al.*, 1994; *Duchêne et al.*, 1997], but this probably involved the collision of microcontinental fragments dispersed within the Neotethys ocean with the active Alpine convergence zone. Full collision with the southern margin of Eurasia probably started in the Paleogene, at about 35–40 Ma [e.g., *Schmid et al.*, 1996].

[1]Department of Earth Sciences, University College London, London, U.K.
[2]Institute of Earth Sciences "Jaume Almera," Consejo Superior de Investigaciones Científicas, Barcelona, Spain.
[3]Netherlands Research Centre for Integrated Solid Earth Sciences, Department of Tectonics, Faculty of Earth and Life Sciences, Vrije Universiteit, Amsterdam, Netherlands.
[4]Department of Geophysics, Faculty of Physics, Universidad Complutense de Madrid, Madrid, Spain.
[5]Now at Department of Earth Sciences, University of Southern California, Los Angeles, California, USA.
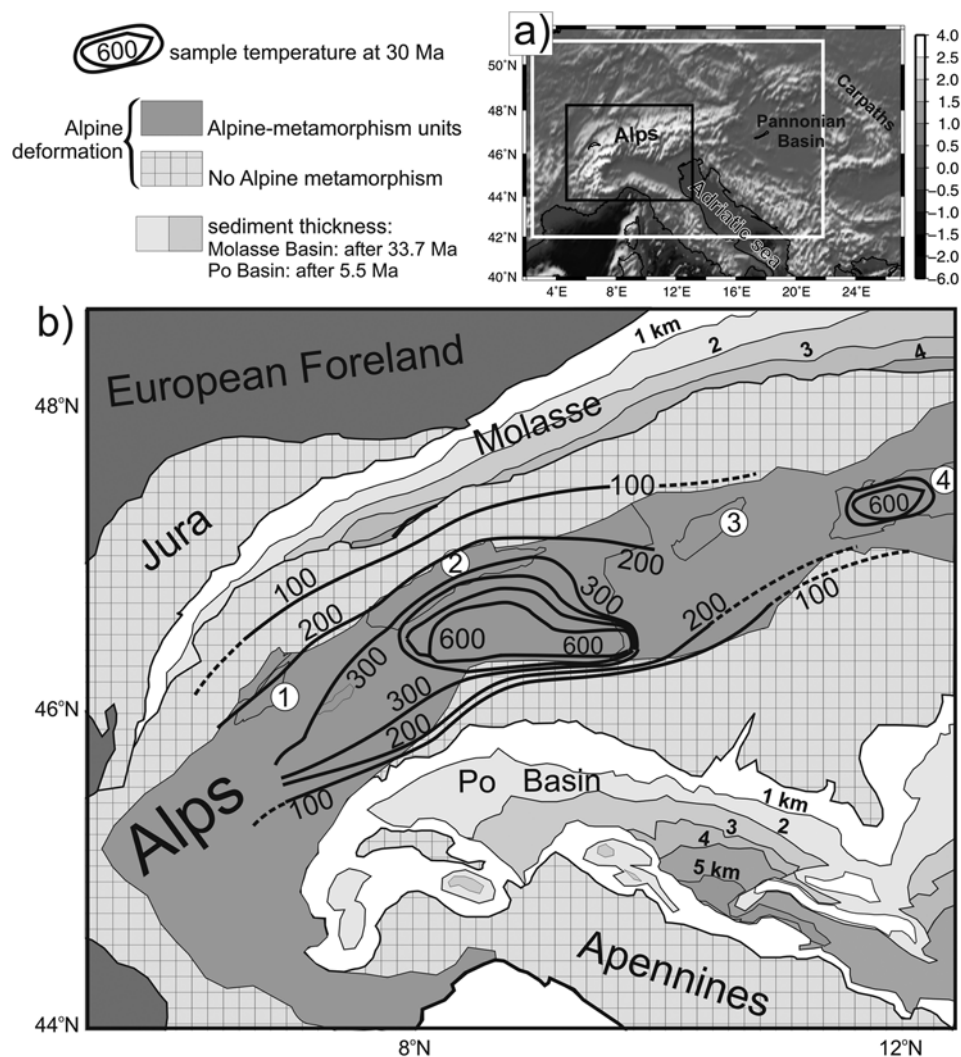
Figure 1. (a) Topography of the Alpine region and location of the modeling area (white rectangle) and the geologic map (black rectangle); (b) geologic map of the study area showing temperature of metamorphic rock samples (black contours, in °C; every 100°C would imply exhumation between 3 and 5 km) at approximately 30 Ma [*Schlunegger and Willett*, 1999; *Hunziker et al.*, 1992]. Gray/white show sediment thickness in the Molasse (Oligocene to present) and Po basins (Pliocene to present) [from *Bigi et al.*, 1990]. Numbers in circles identify the following geological units: 1, Mont Blanc/Aiguilles Rouges massif; 2, Aar Massif; 3, Engadine Window; and 4, Tauern Window.

[5] There is considerable controversy concerning the formation of the west facing arc of the western Alps, and the east facing Carpathian arc, in the context of Alpine collision. Ideas that have been proposed to explain the formation of the western Alpine arc invoke (1) radial thrusting due to a combination of a constant WNW plate motion vector and local body forces [*Platt et al.*, 1989], (2) ring shear or progressive rotation of the Apulian plate and smaller microplates caught up in the collision [*Vialon et al.*, 1989], (3) two successive and differing directions of thrusting due to a change in the plate movement vector [*Ricou and Siddans* 1986; *Laubscher*, 1991], or (4) gravitational collapse of the orogen's sidewall [*Butler et al.*, 1986]. The Carpathian arc, on the other hand, is now generally seen

as an independent system driven by some combination of the forces associated with an eastwardly retreating subducting slab and high gravitational potential energy in the back-arc region [*Sperner et al.*, 2002; *Gvirtzman*, 2002; *Huismans and Bertotti*, 2002].

[6] Much attention has been paid recently to the role of surface processes in shaping the large-scale deformation in orogenic belts. The structural evolution of mountain belts is the result of a critical balance between the rates of lithospheric thickening and surface erosion. Surface mass redistribution produces noticeable pressure changes at deep crustal levels, influencing the timing of fault and rock flow activation and the tectonic evolution of orogens. The dramatic effects of erosion on the evolution of the crustal
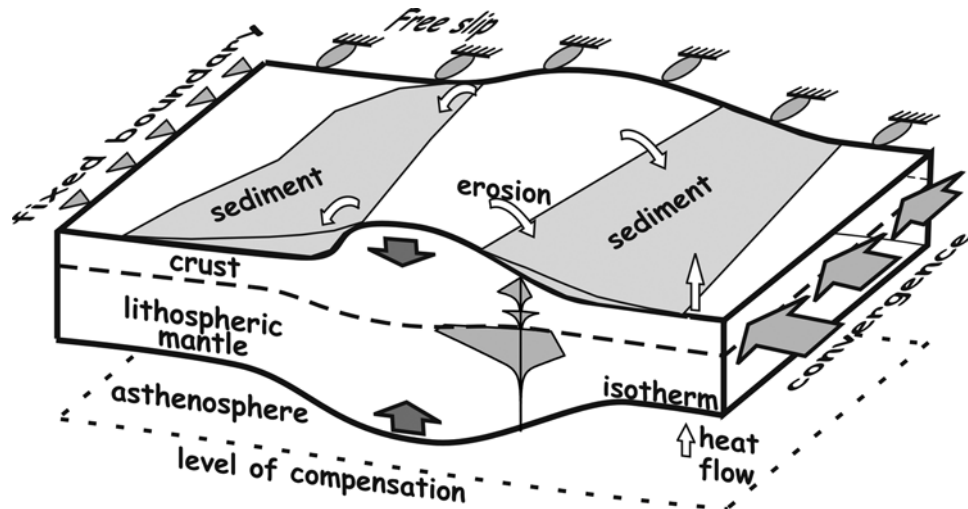
Figure 2. Conceptual cartoon of the numerical model, integrating lithospheric-scale deformation and surface transport. Deformation is computed assuming local isostasy and viscous thin sheet deformation, with a vertically averaged viscosity. Surface sediment transport is approached as a diffusive process.

structure of the Swiss Alps have been discussed on the basis of numerical models by *Pfiffner et al.* [2000]. Surface transport may also prevent collapse of an intracontinental range, as removal of material from topographic heights and deposition in the foreland oppose spreading of the crustal root [*Avouac and Burov*, 1996]. Information concerning sedimentation in the Po (from Pliocene to present) and Molasse (Oligocene to present) basins and exhumation along the Alpine chain is shown in Figure 1. The maximum sediment accumulation on the last 5.5 Myr in the Po basin is 5.5 km [*Bigi et al.*, 1990], implying a maximum sedimentation rate of 1 km Myr^{-1}, whereas the mean rate from Oligocene to present in the Molasse basin is at most 0.12 km Myr^{-1}. Thick contours correspond to temperatures at approximately 30 Ma of metamorphic samples presently at surface [*Hunziker et al.*, 1992; *Schlunegger and Willett*, 1999]. Maximum values of 600°C in the central part of the chain correspond to a total exhumation of about 24 km when assuming a typical thermal gradient of 25° km^{-1}. Little is known about how much of this exhumation is related to erosion or to tectonic processes, but sediment budget studies suggest that about 80% of the total denudation in the core complexes between 22 and 12 Ma is related to tectonic exhumation [*Kuhlemann et al.*, 2001]. Overall, tectonic exhumation is responsible for a minimum of 12% of denudation in the entire Alps since Oligocene.

[7] The thin sheet approach has been widely used to study the large-scale deformation of the lithosphere when it is submitted to external forces. This approach considers the lithosphere as a thin viscous layer [*England and McKenzie*, 1983; *Bird*, 1989; *Jiménez-Munt et al.*, 2005] with vertically averaged rheology subject to plane stresses. Thin sheet models have been applied successfully to understand the role of rheology, for example, during India-Asia convergence [*Neil and Houseman*, 1997], the Iranian plateau [*Sobouti and Arkani-Hamed*, 1996], the central western Europe [*Marotta et al.*, 2001], and the crustal deformation driven by basal velocity [*Ellis et al.*, 1995]. However, they

do not couple lithospheric deformation with surface transport. First results in this direction point to a significant contribution of surface process in controlling the large-scale distribution of lithospheric thickening during orogenesis [*Jiménez-Munt et al.*, 2005] and on the Paleozoic deformation of Australia [*Braun and Shaw*, 2001].

[8] The aim of this work is to find a simple model that can explain the large-scale features of the postcollisional (last 35 Myr) evolution of the Alps, including their planform shape, topography, lithospheric structure, and pattern of erosion/sedimentation, providing an understanding of the processes involved in their development. We pay particular attention to the role of inherited strength contrasts between the Adriatic plate, the European platform, and the region in between.

2. Modeling Approach

[9] We use a finite difference numerical model of lithospheric deformation and erosion/deposition. The mutual interactions among surface transport, viscous lithospheric deformation, and thermal advection and conduction in the lithosphere are accounted for in this fully coupled thermomechanical and surface transport model (Figure 2). The reader is referred to *Jiménez-Munt et al.* [2005] for detailed explanations about the modeling techniques and assumptions, which are summarized here.

[10] To calculate the lithospheric deformation, we adopt a viscous thin sheet approach with vertically averaged viscosity. The thin sheet approach for lithospheric deformation assumes local isostasy and vertical integration of the lithospheric strength to reduce the three-dimensional problem to a planform model, where the horizontal velocity components do not change with depth [*England and McKenzie*, 1983; *Bird*, 1989]. The horizontal velocity field includes the effects of lateral variations of gravitational potential energy related to crustal and lithospheric thickness variations [*Jiménez-Munt et al.*, 2001, 2005]. The calculated velocity

Table 1. Parameters Used in Models

Parameter	Value
Densities for sediments, crust, and asthenosphere (ρ_{sed}, ρ_c, ρ_a); lithospheric mantle $\rho_m = \rho_a \left[1 + (T_{\text{lit}} - T_{\text{moho}})\, \alpha/2\right]$, where T_{moho} is temperature at base of the crust	2450, 2800, 3200 kg m^{-3}
Volumetric thermal expansion of lithospheric mantle (α)	3.5×10^{-5} K^{-1}
Conductivities, sediments, crust, lithospheric mantle, asthenosphere	2.4, 3.0, 3.2, 100.0 W m^{-1} K^{-1}
Heat production, crust, lithospheric mantle (z, depth in km)	$2.5 \exp(-z/15)$, 0 μW m^{-3}
Surface and bottom ($z = 300$ km) temperature	273, 1800 K
Base of the lithosphere, isotherm (T_{lit})	1300°C
Thermal diffusivity	1×10^{-6} m^2 s^{-1}
Rheological	
Upper crust, A [MPa^{-n} s^{-1}], n, Q [kJ mol^{-1}]	2.5×10^{-8}, 3, 138
Lower crust, A [MPa^{-n} s^{-1}], n, Q [kJ mol^{-1}]	3.2×10^{-3}, 3, 251
Lithospheric mantle, A [MPa^{-n} s^{-1}], n, Q [kJ mol^{-1}]	10^3, 3, 523
Dorn law, σ_D [Pa], Q_D [kJ mol^{-1}], $\dot\varepsilon_D$ [s^{-1}]	8.5×10^9, 100, 5.7×10^{11}
Model dimensions	1500×1000 km

field **u** and the assumption of incompressibility provide the changes of crustal thickness s,

$$\frac{\partial s}{\partial t} = \dot\varepsilon_{zz}\, s - \nabla s \cdot \mathbf{u} \tag{1}$$

where $\dot\varepsilon_{zz}$ is the normal component of the vertical strain rate tensor. We calculate the new temperature distribution, which in turn determines the thermal lithospheric thickness and the topography using a local isostasy approach.

[11] The average viscosity and the gravitational potential energy are computed as a function of the temperature distribution in the lithosphere, which is calculated in one dimension for every column of the model. The effective viscosity depends on temperature and strain rate and is calculated from the depth integral of the yield stress envelope. At each depth, the yield stress τ is given by the lesser of the brittle and ductile strengths. The brittle strength is a function of depth, according to $\tau_{\text{brittle}} = \beta z$, where the brittle failure coefficient β is the yield stress gradient depending on the type of fault, the angle of fracture, and the pore pressure. Following *Lynch and Morgan* [1987], this coefficient amounts 16 MPa km^{-1} for extension and 40 MPa km^{-1} for compression. Ductile deformation is governed by a power law creep equation when the applied stresses are less than 200 MPa and by the Dorn law equation for larger stresses. Then, the ductile strength is given by

Power law

$$\tau_{\text{ductile}} = \left(\frac{\dot\varepsilon}{A}\right)^{1/n} \exp\left(\frac{Q}{nRT}\right) \qquad \tau \leq 200 \text{ MPa}$$

Dorn law

$$\tau_{\text{ductile}} = \sigma_D \left\{ 1 - \left[\frac{RT}{Q_D} \ln\left(\frac{\dot\varepsilon_D}{\dot\varepsilon}\right)\right]^{1/2} \right\} \qquad \tau > 200 \text{ MPa} \tag{2}$$

where A, Q, n, σ_D, Q_D, and $\dot\varepsilon_D$ are material constants depending on the rock type, R is the gas constant and T is the absolute temperature (Table 1); $\dot\varepsilon$ is an effective strain rate given by the second invariant of the strain rate tensor

$$\dot\varepsilon = \left(\frac{1}{2}\left(\dot\varepsilon_{xx}^2 + \dot\varepsilon_{yy}^2 + \dot\varepsilon_{zz}^2\right) + \dot\varepsilon_{xy}^2\right)^{1/2} \tag{3}$$

Therefore the effective viscosity η is assumed to be a nonlinear function of local strain rate and temperature,

$$\eta = \frac{\bar\tau}{2\dot\varepsilon}; \qquad \bar\tau = \frac{1}{L}\int_0^L \tau\, dz = \frac{1}{L} F_{Lit} \tag{4}$$

where L is the lithospheric thickness and F_{Lit} is the lithospheric strength (depth integral of the yield stress envelope). Note that this is a purely viscous deformation model; neither elasticity nor plasticity is taken into account.

[12] To calculate erosion and deposition on top of a dynamic topography, surface sediment transport is approached via a diffusive equation:

$$\frac{de}{dt} = K_d \left(\frac{\partial^2 e}{\partial x^2} + \frac{\partial^2 e}{\partial y^2}\right) \tag{5}$$

where K_d is the diffusive coefficient of transport and e is elevation; de/dt is positive for sedimentation and negative for erosion. Inherent to this approach is the assumption that sediment flow is proportional to the local slope, whereas mass conservation during transport implies that the rate of erosion/sedimentation de/dt is proportional to the divergence of mass flow, leading to equation (5). The resulting sediment layer is deformed by the tectonic velocity field in the same way as the crust (equation (1)). Combining these quantitative approaches, the evolution of the elevation e in the model is controlled by the interaction between isostasy, lithospheric thermal evolution, tectonic deformation (thickening/thinning) and erosion/sedimentation.

3. Data and Model Setup

[13] It is now generally recognized that effective numerical modeling of continental deformation must allow for considerable heterogeneity in the strength of continental lithosphere [*Neil and Houseman*, 1997; *Flesch et al.*, 2001]. Such heterogeneity results from the variations in composition and heat flow within the continents [*Watts*, 1992; *Jiménez-Munt et al.*, 2001, 2003]. The structure of the European foreland near the Alps is geologically complicated

and comprises various domains that are likely to differ in bulk strength. The Variscan massifs of central and western Europe (e.g., Bohemian massif, Vosges, Massif Central of France, and the Esterel of SW France) are underlain by plutonic and metamorphic rocks, locally up to granulite facies. These regions are thermally mature, and likely to be of relatively high strength. In contrast, the pre-Alpine southern margin of Europe was affected by rifting during the Mesozoic, which is likely to have significantly reduced its strength [*Watts and Stewart*, 1998; *Watts and Burov*, 2003], and Tertiary rifting along the Rhine and Bresse graben systems is likely to have had a similar weakening effect. A weaker southern edge of the European lithosphere is also suggested by determinations of effective elastic thickness in the North Alpine flexural basin, which produce values ranging from 10 km in the western Alps to 30 km in the east [*Stewart and Watts*, 1997].

[14] In a recent review paper, drawing on the newly compiled Moho map of Europe and constraints on the thermal lithospheric structure from heat flow studies and upper mantle seismic tomography, as well as estimates of the lithospheric thickness from seismological studies, *Cloetingh et al.* [2005] constructed a 3-D strength map of the lithosphere of a large part of Europe. According to their results, the lithospheric strength would increase a factor of 5–10 in the far NW. Also, on the basis of the thermal and mechanical structure along the European Geotraverse, *Okaya et al.* [1996] evaluated the integrated strength of the lithosphere obtaining higher values in Europe than in the central Alps.

[15] Several works point to a nearly rigid behavior of the Adriatic lithosphere. Exposures in the southern Alps (Ivrea zone) suggest that it is likely to have a geological history and mechanical properties similar to the Variscan massifs of northwest Europe [*Handy et al.*, 1999; *Rutter et al.*, 1999], and a relatively high strength is borne out by the lack of substantial deformation during the Alpine collision. From *Cloetingh et al.* [2005] and *Okaya et al.* [1996], a pronounced contrast in strength can be noticed between the strong Adriatic indenter and the weak alpine area. Moreover, the low values of surface heat flow measured for the lithosphere of Adria suggest a cold and therefore strong lithosphere [*Jiménez-Munt et al.*, 2003], in agreement with high velocities derived from *P* wave [*Bijwaard and Spakman*, 2000] and surface wave tomography [*Du et al.*, 1998]. A recent viscoelastic flexural analysis of the Tertiary Piedmont basin has found relatively high viscosity values at the NW edge of the Adriatic plate of $1.5-3 \times 10^{24}$ Pa s [*Carrapa and Garcia-Castellanos*, 2005]. Previous studies also used Adria as a rigid block indentation to investigate the Alpine collision by analytical and analogue experiments [*Regenauer-Lieb and Petit*, 1997; *Ratschbacher et al.*, 1991].

[16] Accordingly, we define three rheologically different areas (Figure 3b): the European foreland, the Adriatic plate, and the weaker orogenic region. In order to simulate the different strength of each area we multiply the viscosity given in equation (4) by a factor of 5 in the European foreland, and we impose a viscosity of 10^{25} Pa s in the Adria indenter to force it to behave as a rigid block. Figure 3c shows the initial effective viscosity and resulting vertical strain rate along a NW-SW profile displayed in Figure 3b.

[17] The lower strength of the orogenic region between the stiff European foreland and the Adriatic plate, together with the applied boundary conditions, determine how indentation is dynamically accommodated throughout the region. We have explored different geometries for the indenter and for the boundary between strong and weak lithosphere in the European foreland, and the one we have chosen is the only one that permits proper reproduction of the shape of the region of thickened crust in the Alps and of the pattern of vorticity reflected in paleomagnetically determined vertical axis rotations.

[18] For simplicity, we have assumed initially uniform crustal and lithospheric thicknesses. A representative average value of 30 km for the crustal thickness has been assumed on the basis of tectonic reconstructions for early Oligocene time [*Platt*, 1986]; this value coincides with the present-day crustal thickness of the European foreland [e.g., *Dèzes and Ziegler*, 2001]. The value of 100 km adopted for the lithospheric thickness, together with the local isostasy assumption and the parameters listed in Table 1, results in

Figure 3. (a) Restoration of displacements in the Alps in terms of the relative motions of discrete terrains. Displacement estimates are from *Platt* [1986] and *Menard et al.* [1991]. (left) Restoration of the Helvetic phase of deformation from 35 to 6 Ma. The 145 km displacement of Adria at 304° relative to Europe is partitioned into right-lateral motion between Adria and the central/eastern Alps along the Insubric fault and northward motion of the central/eastern Alps relative to Europe creating the Helvetic thrust belt. In the western Alps the displacement is partitioned into SE directed thrusting along the margin with Adria and WNW thrusting in the sub-Alpine fold belt. The western Alps and the central/eastern Alps are treated as separate terrains, with WSW directed relative motion along the Simplon normal fault. Vector triangles for the three systems are shown as insets. (right) Restoration of the Jura phase of deformation since 6 Ma, which reflects WNW displacement of the Alps relative to Europe (creating the Jura fold belt), and NW displacement of Adria with respect to the southern Alps) producing the Orobic fold belt. The net displacement of Adria with respect to Europe is 85 km at 308° (inset vector diagram). (b) Model setup showing the initial geometry and applied boundary conditions from 35 to 6 Ma (black solid arrows) and from 6 Ma to present (grey arrows). These conditions are designed to produce a continuous velocity field that corresponds as closely as possible to the displacement vectors shown in Figure 3a. White arrows at the eastern boundary represent the opening of the Pannonian basin in the period from 22 to 8 Ma. Rollers represent free slip on this boundary and triangles null fixed velocity. The model domain is 1500 × 1000 km, and corresponds to the area between (2.2°E, 41.8°N) and (22°E, 51°N). (c) Initial effective viscosity η and resulting vertical strain rate $\dot{\varepsilon}_{zz}$ along a NW-SW profile located in Figure 3b.

an elevation of 325 m [*Jiménez-Munt et al.*, 2001]. The horizontal dimensions of the modeled domain are 1500 km from west to east and 1000 km from north to south, with grid horizontal spacing of 15 km. This domain corresponds to the region from 41.8°N to 51°N and from 2.2°E to 22°E.

[19]   Relative plate motions between Africa and Eurasia, paleostress fields in the European platform, and intraorogenic displacements [*Platt et al.*, 1989; World Stress Map, available at http://www.world-stress-map.org] all constrain the Oligocene-Miocene motion of the Adria indenter. Taking into account all these studies and the block movements obtained from shortening measurements [*Menard et al.*,

1991], we have estimated the rotation velocity of Adria at different stages. We have deduced averaged displacement vectors of 145 km length and azimuth 304° from 35 to 6 Ma and 85 km at 308° from 6 Ma to present, as representative of the mean motion of Adria with respect to a fixed Europe (Figure 3a). From these vectors we have computed a constant location of the Euler pole at (7.1°E, 39.3°N) and counterclockwise angular velocities of 1.5° Myr^{-1} from 35 to 6 Ma (black arrows in Figure 3b), and 2.5° Myr^{-1} from 6 Ma to the present (grey arrows in Figure 3b). These values are converted into tangential velocities that are applied to the eastern part of the southern boundary of the model
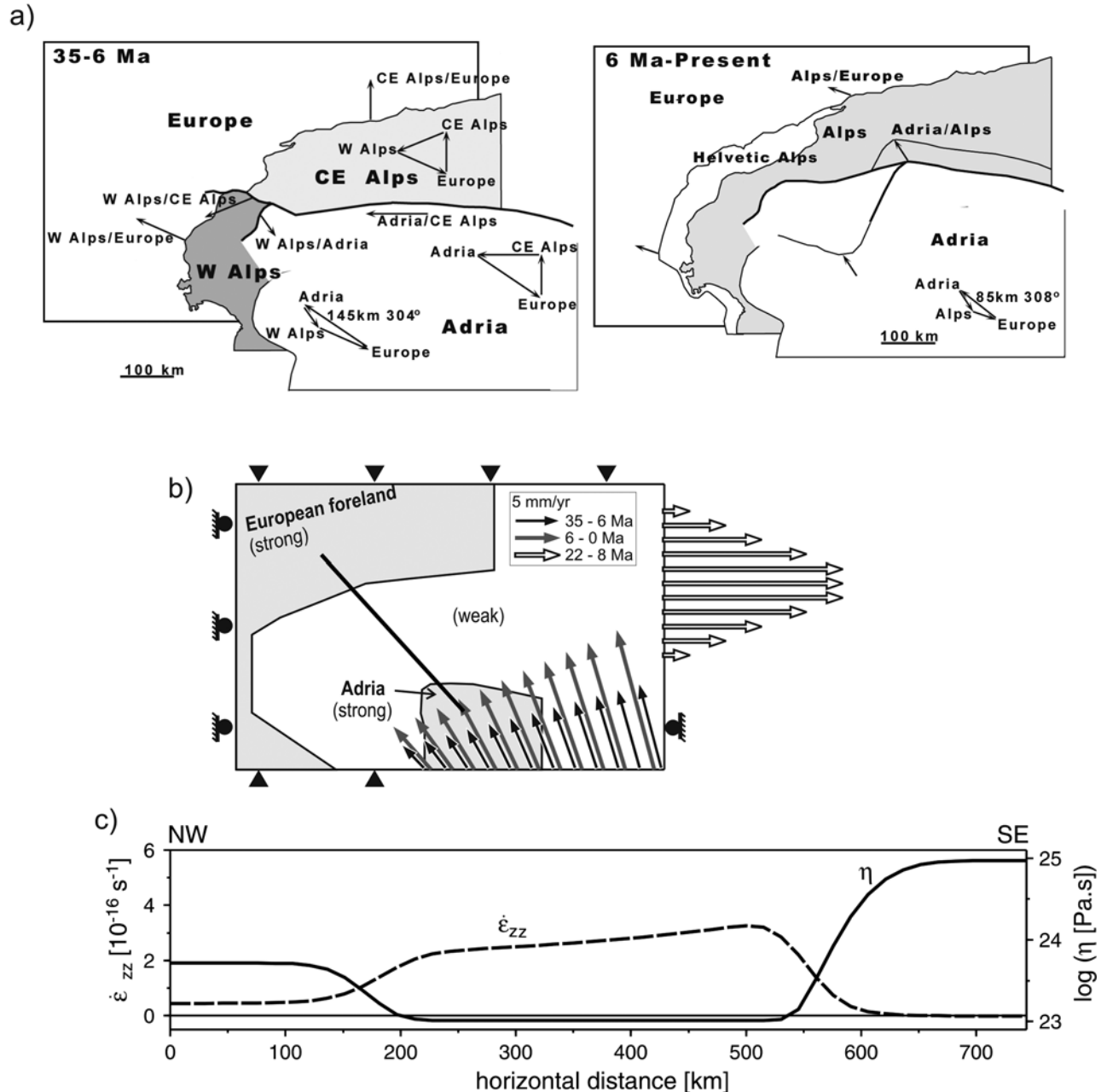

Figure 3

domain to simulate indentation (Figure 3b). The eastward velocities on the eastern boundary (white arrows in Figure 3b) represent the eastward retreat of the Carpathian arc, and they are applied only between 22 and 8 Ma [*Horvath*, 1993].

4. Results

[20] Figure 4 shows modeling results for the present-day situation, which correspond to the final stage of model evolution. Here we investigate the effects of the viscosity dependence on strain rate and of surface (erosion/sedimentation) processes. We disregard erosion and sedimentation in models A and B. In model A, to calculate the viscosity, we consider a constant value of effective strain rate (4 × 10^{-16} s^{-1}) through the entire model domain, and therefore lateral variations of viscosity within an area are due only to temperature variations. In contrast, in models B and C we consider that viscosity depends both on temperature and local value of effective strain rate given by equation (4).

[21] Model A fails to concentrate deformation in a narrow area, and in consequence, it results in low elevation and crustal and mantle lithosphere thicknesses (Figures 4a−4c and 5a). Although these values increase when decreasing the assumed strain rate, the model still fails to reproduce the geometry of the chain. Instead, model B properly reproduces the main features of the chain and predicts maximum topography and Moho depth of about 3700 m and 61 km in the central Alps (Figures 4d−4f).

[22] Including the effects of erosion and sedimentation leads to significant improvement of modeling results (model C, Figures 4g−4j) because the maximum predicted elevation now occurs in the western Alps, with values of about 2700 m, in good agreement with averaged topography in the same area. The reason for the shifting of maximum elevation toward the west (compared to model B) is that erosion reaches maximum amounts in the central Alps of about 8 km (Figure 4j) as a result of higher topographic gradients in that area. These high gradients are in turn imposed by the rotation of Adria and its proximity to Europe in the central Alps. Erosion produces a reduction of about 5 km of the maximum predicted Moho depth, which reaches maximum values of 53 km, in agreement with recent maps of Moho depth [*Dèzes and Ziegler*, 2001; *Waldhauser et al.*, 2002]. In contrast, the lithospheric mantle becomes slightly thicker under the orogen when erosion is included [*Jiménez-Munt et al.*, 2005]. We use a value of K_d = 1000 m^2 yr^{-1}

corresponding to moderate to high erosion rates. This value has been chosen as a compromise to maximize the predicted erosion while keeping a reasonable topography and crustal thickness. Figure 5a shows that higher values of diffusivity K_d induce little increase in erosion and total transport. The mean amount of erosion of about 5 km predicted in model C accounts for most of the mean overall erosion in the Alps derived from thermochronological studies (5 km imply 125°C in Figure 1 if assuming a thermal gradient of 25°C km^{-1}). This in rough agreement with the results by *Kuhlemann et al.* [2001] that up to 88% of post-Oligocene denudation in the entire Alps is due to erosion rather than tectonic exhumation. The location of the maximum predicted erosion (8 km) in the central part of the chain is consistent with the location of maximum exhumation in the Tauern Window (Figure 1) but about 3 times smaller in magnitude [see also *Kuhlemann et al.*, 2001, and references therein]. However, the satisfactory fit of the observed tectonic shortening and final crustal thickness ensures that overall erosion in the Alps could not be much higher than predicted in our model. Therefore our results suggest that most exhumation observed at the Engadine and Tauern windows (about 24 km if assuming a thermal gradient of 25°C km^{-1}) is tectonically induced, likely by synorogenic to late orogenic extension causing tectonic exhumation [*Platt*, 1986; *Kuhlemann et al.*, 2001]. The model-predicted sediment thickness is higher in the southern margin of the Alps than in the northern side, in good agreement with the observed pattern of sedimentation (Figure 1). Values of about 5 and 2.4 km are obtained in the Po and Molasse basins, respectively. This asymmetric pattern of sedimentation is mainly due to the arcuate shape of the chain. Similarly, the model correctly predicts a sediment thickness increase from west to east in the Molasse basin, as a result of the decrease of the planform curvature of the orogen in the same direction.

[23] Model-predicted sediment thickness clearly underestimates observations, especially keeping in mind that the modeled period is 5−6 times longer than the age range of sediments displayed in Figure 1 for the Po basin. This misfit might be due to the sediment contribution of the Apennines, which is not included in our modeling, and the fact that we are not considering the flexure of the lithosphere. Furthermore, numerical simulations demonstrate that sediment transport to a foreland basin cannot be explained with a local isostatic approach because flexural subsidence of the basin is needed to generate accommodation space for the

---

Figure 4. Model results at the last stage (35 Myr, corresponding to the present) for (left) model A, temperature-dependent viscosity and constant effective strain rate of 4 × 10^{-16} s^{-1} thorough the entire model domain; (middle) model B, temperature- and strain rate-dependent viscosity; and (right) model C, same as model B but incorporating erosion and sedimentation, K_d = 1000 m^2 yr^{-1}. (a−c) Actual topography in the study area (color shading) and the model-predicted topography (contours). (d−f) Predicted Moho depth and (g−i) lithospheric mantle thickness (vertical distance between the 1300°C isotherm and the Moho). (j) Amount of erosion/sedimentation predicted in model C (negative values for erosion and positive for sedimentation). The coastline of the study area is plotted for reference. Note that the three models incorporate the same boundary conditions and therefore the same amount of mass input and total lithospheric shortening. Differences in topography and thickness distributions are due exclusively to the different rheology assumed (compare models A and B) and to the effects of surface transport (compare models B and C). See color version of this figure at back of this issue.
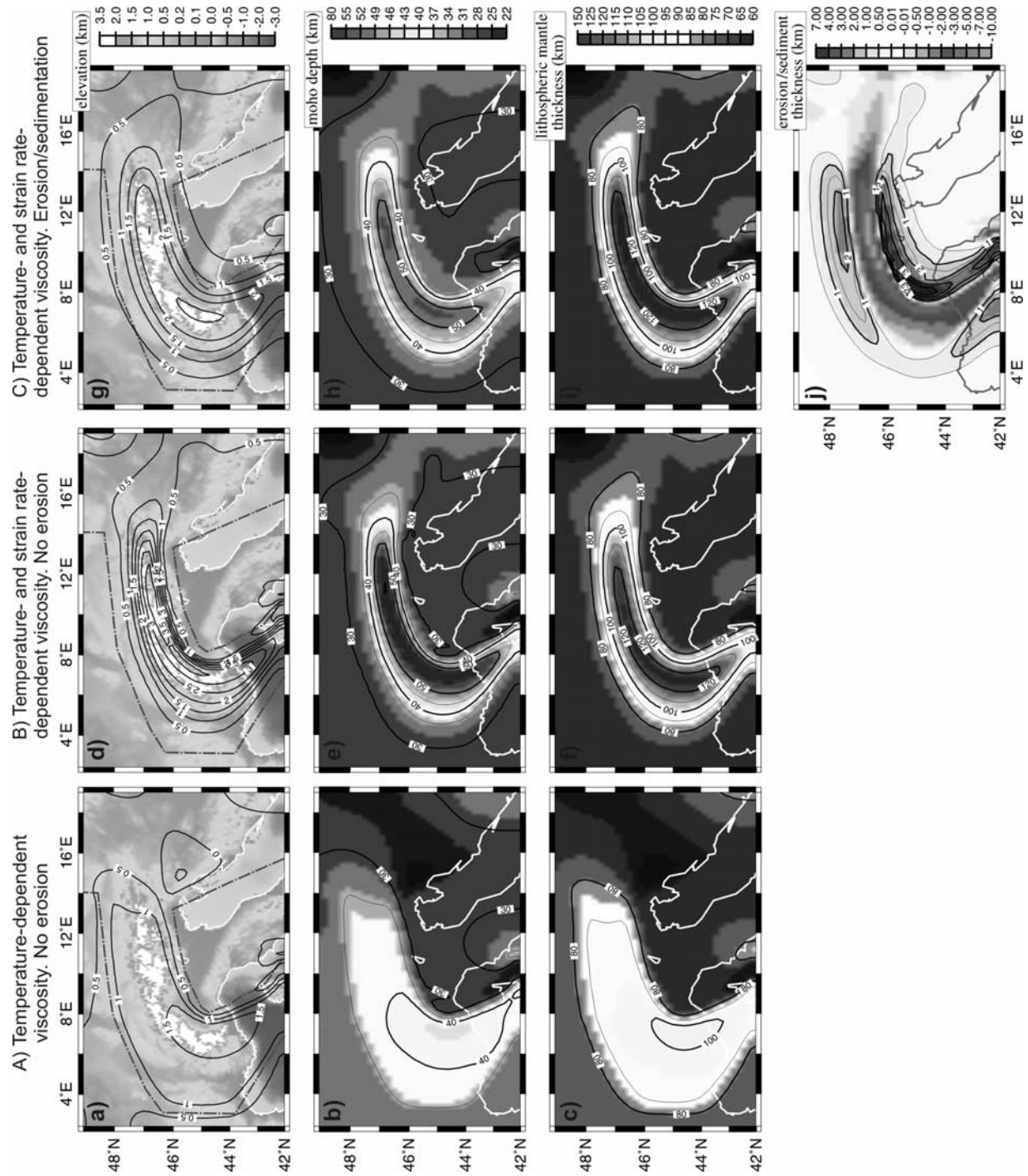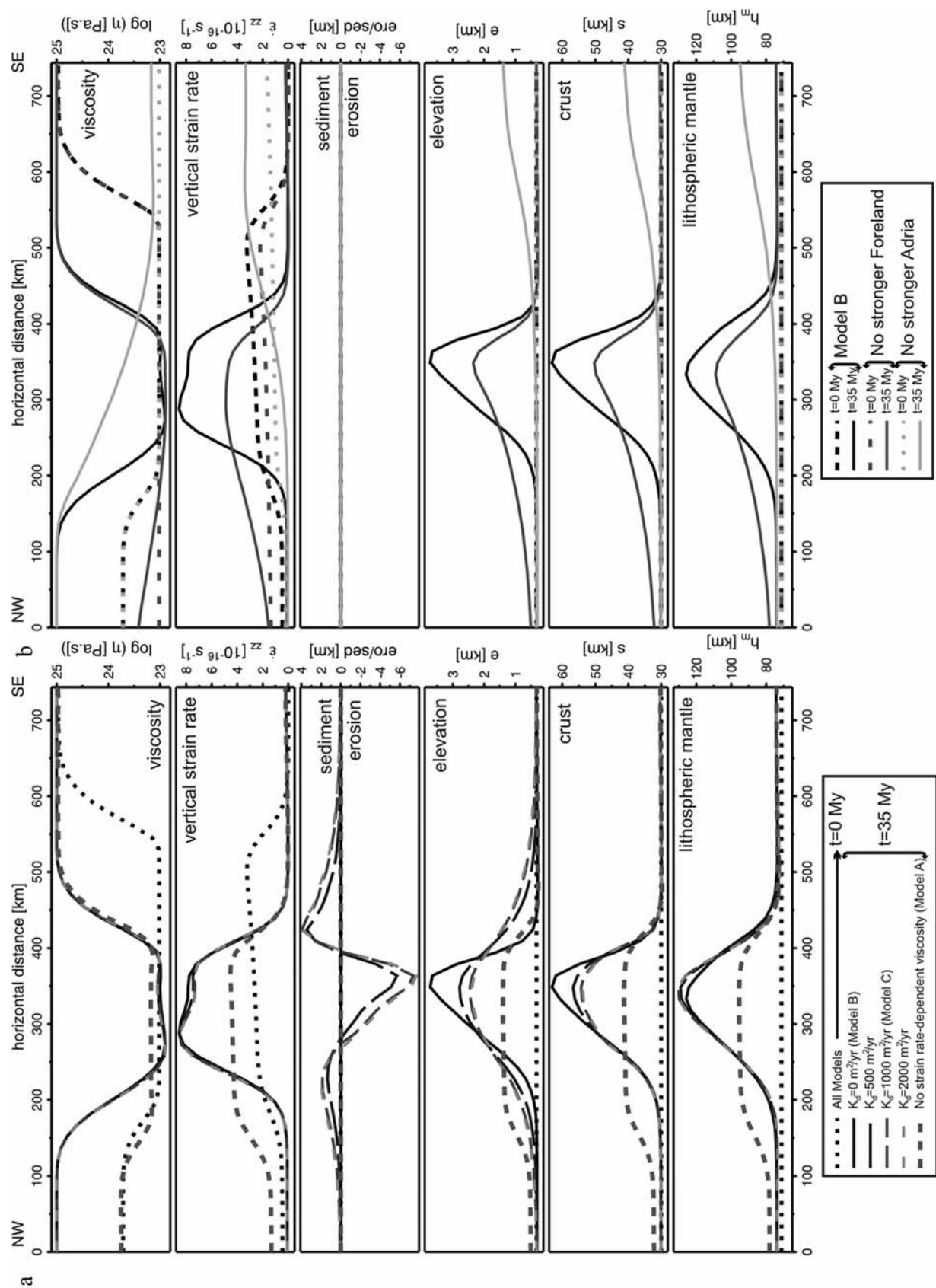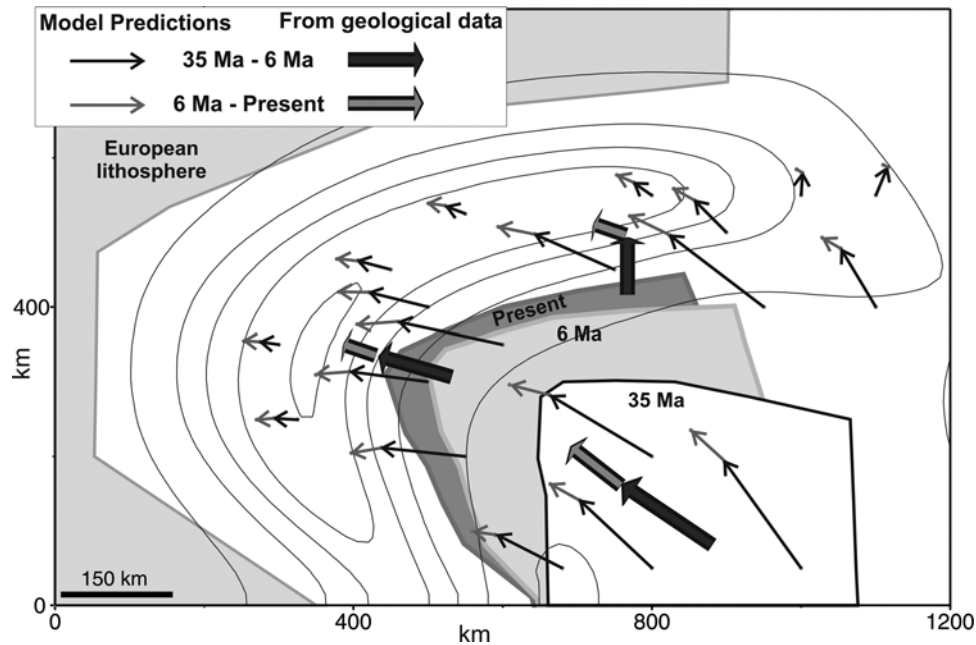
Figure 4

Figure 5

Figure 6. Displacements within the model domain predicted with model C. Vectors between positions at 35 to 6 Ma and 6 Ma to present are compared to those deduced from geologic studies (Figure 3a and here thick arrows). White and grey arrows correspond to the first and second stages, respectively. White grey areas indicate model resulting positions of Adria at 35 Ma, 6 Ma, and present.

sediments [*Garcia-Castellanos*, 2002]. In fact, our model predicts relevant sediment accumulations only because a diffusive model of surface transport is applied, whereas a more realistic fluvial transport model would result in a lower sediment accumulation in absence of lithospheric flexure. Because we need to assume local isostasy for the thin sheet calculations, we opt for neglecting flexural isostasy and using a simplistic diffusive transport model. However, it must be kept in mind that the absolute values of predicted sediment thickness are not to be compared with observations, and the relative predicted variations discussed above must be taken with caution.

[24] In order to produce a region of thickened crust and elevated topography resembling the present Alpine chain we need to concentrate the deformation in front of Adria, which requires definition of three different rheological areas. Figure 5b shows that if we assume a foreland with the same rheology as the orogenic region, the strain is distributed over the whole European platform, resulting in lower final topography and crustal thickness in the Alpine region. Moreover, unless Adria is very strong relative to its surroundings, the deformation is also distributed within Adria, producing the highest topography close to the southern boundary, where the velocity condition is imposed in the model. These results are in agreement with that

obtained by *Ratschbacher et al.* [1991], where they show that the best experiments are those with a narrow width of the deformable area and a rigid foreland.

[25] Different initial geometries yield results that differ only slightly from those described below. For example, assuming an initial crustal thickness of 40 km in only the intermediate area results in an initial elevation of 1500 km and a reduction in the effective viscosity to 45% in the area. This also produces an increase in the total eroded and sediment volume by 35%; however, it does not change the main conclusions derived from the model described in this section. Finally, note that all models fail to reproduce the southwestern termination of the Alps because they neglect the postorogenic opening of the Ligurian basin and probably because they assume uniform initial topography and indenter edge effects.

[26] The predicted displacements between 35 and 6 Ma and 6 Ma to present of some selected points are in reasonable agreement (Figure 6) with geological reconstructions (Figure 3a) [*Platt*, 1986; *Platt et al.*, 1989; *Menard et al.*, 1991]. The model predicts northwestward displacements of about 150 km of Adria from 35 to 6 Ma and nearly 100 km from 6 Ma to the present. Westward displacement of the western Alps is also in good agreement with geological observations. However, our viscous thin sheet

Figure 5. NW-SE profiles (located in Figure 3b) of model variables at different stages. From top to bottom, effective viscosity, vertical strain rate, accumulated erosion (negative values) and sedimentation (positive), elevation, crustal thickness (sediments excluded), and lithospheric mantle thickness. (a) Models with different K_d and nonstrain rate-dependent viscosity; (b) models with no strength contrast with the European foreland (grey lines) and no strength contrast with Adria (clearer lines).
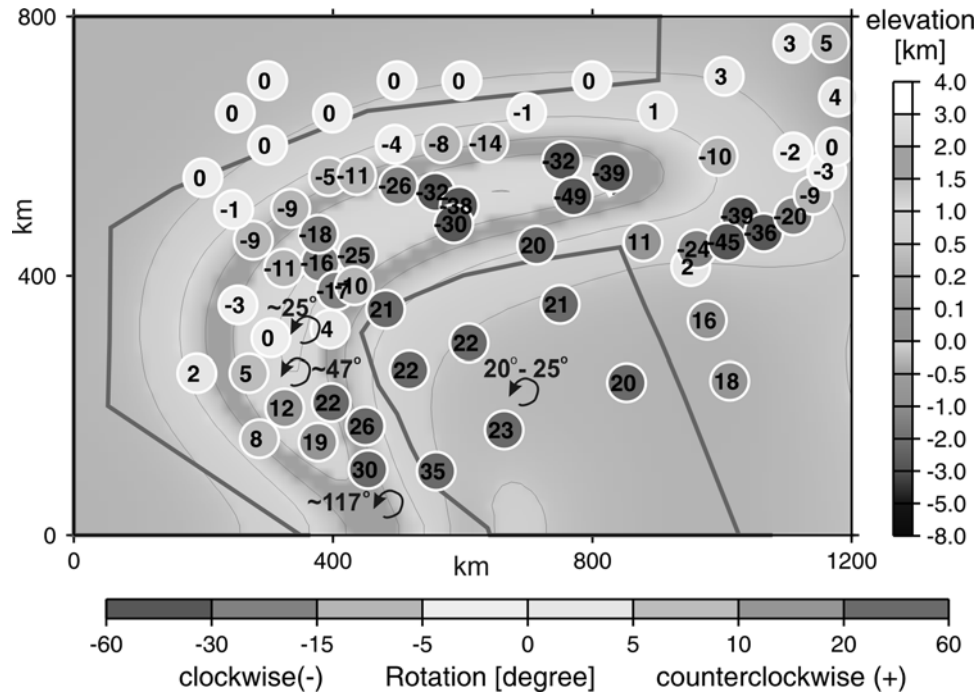
Figure 7. Vertical axis rotations predicted by the model C since 35 Ma (color circles). These are compared with paleomagnetic measurements for the western Alps since the Oligocene (black arrows and numbers [*Collombet et al.*, 2002]). Blue and red indicate clockwise and counterclockwise rotation, respectively. See color version of this figure at back of this issue.

model is not able to reproduce the observed northward motion of the central Alps from 35 to 6 Ma. This is due to the lack of fault deformation in our numerical model, failing to incorporate the dextral relative motion along the Giudicarie transform fault.

[27] The model also predicts a distribution of vertical axis rotations (Figure 7). The finite rotation, θ, is obtained by integrating with time half of the vertical component of the vorticity of the viscous thin sheet flow,

$$\theta = \frac{1}{2} \int \left(\frac{\partial v}{\partial x} - \frac{\partial u}{\partial y} \right) dt,$$

where u, v are the horizontal components of the velocity and t is time.

[28] The geometry assumed for the European foreland and the Adriatic indenter, together with the northwestward motion of the indenter, causes clockwise rotations in the central and eastern Alps and counterclockwise rotation of

the western Alps. These predictions, and the increase of vertical axis rotation toward the southwestern Alps, are in good agreement with rotations since the Oligocene deduced from paleomagnetic data [*Collombet et al.*, 2002]. The geometry of the western foreland helps to produce this increasing counterclockwise rotation toward the southwest. Our viscous deformation model underestimates the maximum values of rotation, which occur where elongate fault-bounded blocks are oriented at high angles to the local shear direction, whereas our model predicts regionally averaged values of rotation.

[29] In order to constrain the mechanisms responsible for the present-day deformation pattern, we apply two end-member sets of boundary conditions for the last 0.2 Myr. In Figure 8 we show a comparison of the horizontal components of the principal strain rate tensor obtained by testing both sets of boundary conditions and the effect of the gravitational potential energy (GPE) variations for the present-day situation.

Figure 8. Horizontal components of the principal strain rate tensor predicted for the last stage (present-day) of model C (arrows for extension and bars for compression). Inset 1 corresponds to the boundary condition without Adria movement and applied on Figure 8a; and inset 2 shows present rotation of Adria, the velocity boundary conditions are computed assuming an Euler pole from a geodetic study [*Calais et al.*, 2002] and applied on Figures 8b and 8c. The strain rates are obtained considering: (a) the only driving force that comes from lateral variations of GPE, no Adria convergence (inset 1); (b) by applying in an homogeneous lithosphere (no lateral variations of crustal and lithospheric thickness, therefore, no lateral contrast of GPE) a velocity boundary condition is computed from the present Euler pole (inset 2); and (c) by applying to the last stage (including the lateral variations of GPE) the velocity boundary condition is computed from the same Euler pole (inset 2). Contours correspond to the predicted elevation.
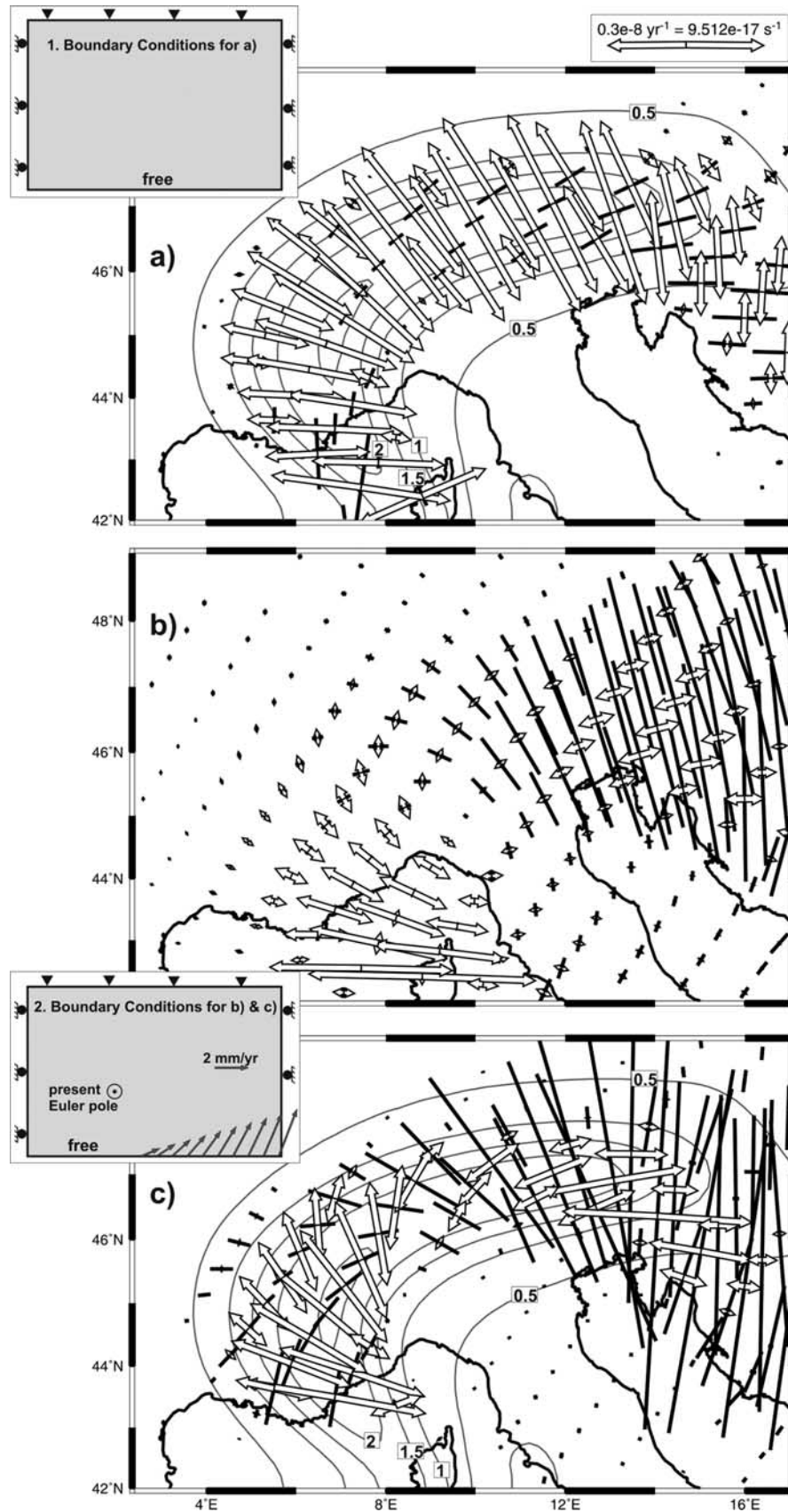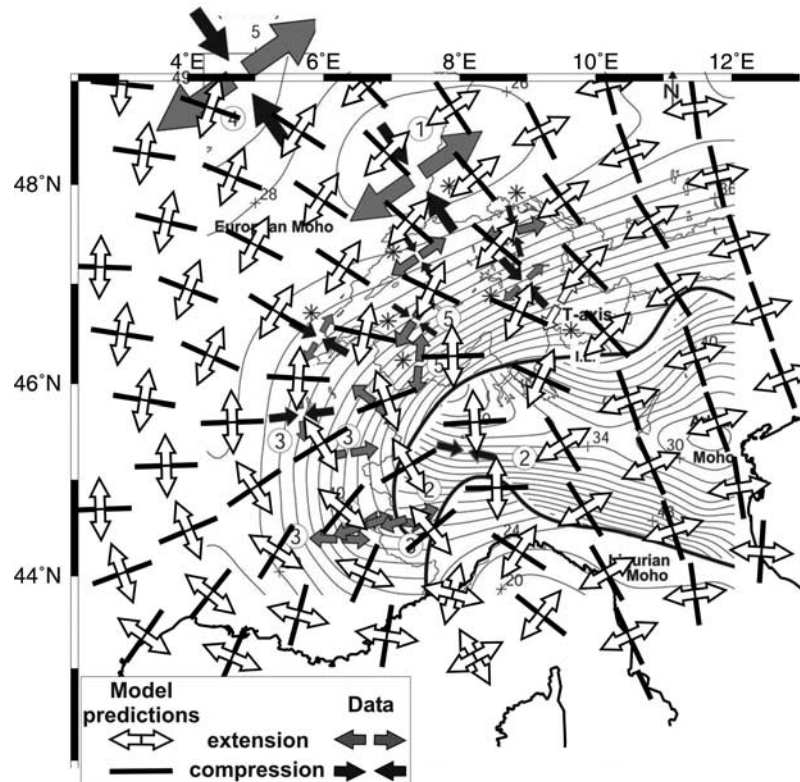
Figure 8

Figure 9. Horizontal components of the principal strain rate directions, predicted by thin sheet model C (black bars for compression and white arrows for extension) and measures compiled by *Kastrup et al.* [2004] (black arrows for compression and grey arrows for extension). Contours are Moho depth, with 2 km interval [*Waldhauser et al.*, 2002].

[30] If we assume no convergence between Adria and Europe during the last 0.2 Myr (Figure 8a), then the only driving force is related to lateral variations of GPE, caused by lateral contrasts in topography and crustal and lithospheric mantle thicknesses. In the absence of applied convergence, these variations in GPE cause horizontal extension nearly perpendicular to the strike of the chain, although with a very low strain rate. A remarkable feature is that the maximum rate of extension does not correspond strictly to the region of maximum topography. This is due to the contribution of variations in the thickness of lithospheric mantle in the calculation of GPE.

[31] In the last few years, several geodetic measurements have been carried out in the Alps and along the Italian Peninsula, and some authors have used these studies to determine the present pole of rotation of Adria relative to Eurasia [*Calais et al.*, 2002; *Battaglia et al.*, 2004]. These works treat the plates as rigid blocks and therefore disregard deformation due to the lateral contrasts of GPE. The strain rate distribution shown in Figure 8b is the result of applying the counterclockwise rotation of Adria relative to Europe in a homogeneous lithosphere (no lateral changes of crustal and lithospheric thickness) so that no deformation is produced by lateral contrasts of GPE. The convergence is calculated using the Euler pole obtained in the geodetic study by *Calais et al.* [2002], with pole location at 45.36°N/ 9.10°E (near Milan) and angular rate of 0.52° Myr^{-1}, which

is very similar to the pole obtained in other geodetic and seismological studies [*Battaglia et al.*, 2004, and references therein]. Using this rotation pole, the resulting boundary conditions are shown in inset 2 of Figure 8. The assumed present-day Euler pole is very different from that considered for the last 6 Myr, resulting in a lower rate of convergence in the Alps. Under these conditions, the horizontal extension rotates clockwise from the western to the eastern part, with predominant NW-SE extension in the west and nearly N-S compression to the east.

[32] Finally, we calculate the strain rate tensor taking into account both effects, the deformation due to the variations of GPE and that due to counterclockwise rotation of Adria (Figure 8c). Again we obtain a progressive rotation in the direction of extension from perpendicular to the strike of the chain in the west to parallel to it in the eastern Alps (Figures 8b and 8c). However, including the lateral contrast of GPE (Figure 8c) causes an increase in the magnitude of the extensional component along the chain. This is consistent with the state of stress determined from focal mechanisms by *Kastrup et al.* [2004] (Figure 9). We also obtain a change in tectonic regime from normal faulting in the southwest to thrusting in the eastern Alps.

[33] The predicted strike-perpendicular extension in the western Alps is also in good agreement with strain rates deduced from triangulation of a local GPS network [*Calais et al.*, 2002], although caution must be taken considering

the large uncertainty of the geodetic velocity vectors and the simplifying assumptions made here. This modeling suggests that the present-day extension observed in the western Alps can be explained mainly in terms of lateral variations of GPE in this area. This result agrees with the observations and stress/strain analyses done by *Delacou et al.* [2004] which imputes the current activity on the western Alps mostly as a result of gravitational ''body'' forces. However, a counterclockwise rotation of Adria relative to Europe (with the Euler pole to the south and close to the plate boundary) is needed to explain the present-day strike slip and transpression observed in the central and eastern Alps (Figure 9).

5. Conclusions

[34] The postcollisional evolution of the Alps is controlled by accommodation of convergence in a weak zone caught in between a nearly rigid Adria plate and a strong European foreland. Model results are strongly sensitive to the assumed rheology. A nonlinear strain rate-dependent rheology is required to reproduce the correct shape of the Alpine chain. In contrast, models assuming either a constant viscosity within each region or a viscosity that only depends on temperature produce more widely distributed deformation than is observed and hence lower elevation and crustal thickness.

[35] Surface mass transport processes are shown to play a significant role in the evolution of the Alpine chain. The model is consistent with a mean erosion of 4–7 km in the entire Alps with maximum values of 8 km in the central Alps. These values confirm that at the scale of the entire Alps erosion is responsible for most of the exhumation, whereas tectonic exhumation is dominant only in the core complexes. Neglecting surface transport can lead to signif-

icant overestimation of maximum Moho depth and topography and to underestimation of maximum lithospheric mantle thickness. Surface processes are also needed to determine the correct location of the maximum topography (in the west) and maximum rock exhumation (in the central Alps), arising from lower average topographic gradients occurring in the west. The larger sediment accumulation in the southern side of the Alps (Po basin) relative to the northern side (Molasse basin) is mainly related to the arcuate geometry of the Alps resulting from the indentation of the Adriatic plate.

[36] The present-day strike-perpendicular extension observed in the western Alps can be explained as driven by lateral variations of GPE in this area. Ongoing rotation of Adria relative to Europe causes the observed rotation of extension direction from perpendicular to the chain in the western Alps to parallel to it in the eastern Alps. In this way, we obtain a change in tectonic regime from normal faulting in the southwestern Alps to thrusting in the eastern Alps. Whereas explaining this present stress regime requires a rotation pole similar to that derived from geodetic measurements (9.10°E, 45.36°N), a rotation pole further to the south (7.1°E, 39.3°N) is needed to reproduce the distribution of mean postcollisional Alpine deformation. Consequently, we propose that the Euler pole of Adria (relative to Europe) has shifted NNE about 700 km from the location responsible for mean postcollisional deformation to the present-day situation.

References

Avouac, J. P., and E. B. Burov (1996), Erosion as a driving mechanism of intracontinental mountain growth, *J. Geophys. Res.*, *101*, 17,747–17,769.

Battaglia, M., M. H. Murray, E. Serpelloni, and R. Burgmann (2004), The Adriatic region: An independent microplate within the Africa-Eurasia collision zone, *Geophys. Res. Lett.*, *31*, L09605, doi:10.1029/2004GL019723.

Bigi, G., et al. (1990), Current plate motions, *Geophys. J. Int.*, *101*, 425–478.

Bijwaard, H., and W. Spakman (2000), Non-linear global P-wave tomography by iterated linearized inversion, *Geophys. J. Int.*, *141*, 71–82.

Bird, P. (1989), New finite element techniques for modeling deformation histories of continents with stratified temperature-dependent rheology, *J. Geophys. Res.*, *94*, 3967–3990.

Braun, J., and R. Shaw (2001), A thin plate model of Paleozoic deformation of the Australian lithosphere: Implications for understanding the dynamics of intracratonic deformation, in *Continental Reactivation and Reworking*, edited by J. Miller et al., *Geol. Soc. Spec. Publ.*, *184*, 165–193.

Butler, R. W. H., S. J. Matthews, and M. Parish (1986), The NW external Alpine thrust belt and its implications for the geometry of the western Alpine orogen, in *Collision Tectonics*, edited by M. P. Coward and A. C. Ries, *Geol. Soc. Spec. Publ.*, *19*, 245–260.

Calais, E., J.-M. Nocquet, F. Jouanne, and M. Tardy (2002), Current strain regime in the western Alps from continuous GPS measurements, 1996–2001, *Geology*, *30*, 651–654.

Carrapa, B., and D. Garcia-Castellanos (2005), Western Alpine back-thrusting as subsidence mechanism in the western Po Basin, *Tectonophysics*, *406*, 197–212.

Channell, J. E. T., B. D'Argenio, and F. Horvath (1979), Adria, the African promontory, *Earth Sci. Rev.*, *15*, 213–292.

Cloetingh, S., et al. (2005), Lithospheric memory, state of stress and rheology: Neotectonic controls on Europe's intraplate continental topography, *Quat. Sci. Rev.*, *24*, 241–304.

Collombet, M., J. C. Thomas, A. Chauvin, P. Tricart, J. P. Bouillin, and J. P. Gratier (2002), Counterclockwise rotation of the western Alps since the Oligocene: New insights from paleomagnetic data, *Tectonics*, *21*(4), 1032, doi:10.1029/2001TC901016.

Delacou, B., C. Sue, J.-D. Champagnac, and M. Burkhard (2004), Present-day geodynamics in the bend of the western and central Alps as constrained by earthquakes analysis, *Geophys. J. Int.*, *158*, 753–774.

Dewey, J. F., M. L. Helman, E. Turco, D. H. W. Hutton, and S. D. Knott (1989), Kinematics of the western Mediterranean, in *Alpine Tectonics*, edited by M. P. Coward, D. Dietrich, and R. G. Park, *Geol. Soc. Spec. Publ.*, *45*, 421–443.

Dèzes, P., and P. A. Ziegler (2001), European map of the Mohorovicic discontinuity, paper presented at 2nd EUCOR-URGENT Workshop (Upper Rhine Graben Evolution and Neotectonics), Mt. St. Odile, France.

Du, Z. J., A. Michelini, and G. F. Panza (1998), EurID: A regionalized 3-D seismological model of Europe, *Phys. Earth Planet. Inter.*, *105*, 31–62.

Duchêne, S., J. Blichert-Toft, B. Luais, P. Telouk, J.-M. Lardeaux, and F. Albarède (1997), The Lu-Hf dating of garnets and the ages of the Alpine high-pressure metamorphism, *Nature*, *387*, 586–589.

Ellis, S., P. Fullsack, and C. Beaumont (1995), Oblique convergence of the crust driven by basal forcing: Implications for length-scales of deformation and strain partitioning in orogens, *Geophys. J. Int.*, *120*, 24–44.

England, P., and D. P. McKenzie (1983), Correction to: A thin viscous sheet model for continental deformation, *Geophys. J. R. Astron. Soc.*, *73*, 523–532.

Flesch, L. M., A. J. Haines, and W. E. Holt (2001), Dynamics of the India-Eurasia collision zone, *J. Geophys. Res.*, *106*, 16,435–16,460.

Froitzheim, N., S. S. Schmid, and P. Conti (1994), Repeated change from crustal shortening to orogen-parallel extension in the Austroalpine units of Graubünden, *Eclogae Geol. Helv.*, *87*, 559–612.

Garcia-Castellanos, D. (2002), Interplay between lithospheric flexure and river transport in foreland basins, *Basin Res.*, *14*, 2, 89–104.

Gvirtzman, Z. (2002), Partial detachment of a litho-spheric root under the southeast Carpathians: Towards a better definition of the detachment concept, *Geology*, 30, 51–54.

Handy, M. R., L. Franz, F. Heller, B. Janott, and R. Zurbriggen (1999), Multistage accretion and exhumation of the continental crust (Ivrea crustal section, Italy and Switzerland), *Tectonics*, 18, 1154–1177.

Horvath, F. (1993), Towards a mechanical model for the formation of the Pannonian Basin, *Tectonophysics*, 226, 333–357.

Huismans, R. S., and G. Bertotti (2002), The Transylvanian basin, transfer zone between coeval extending and contracting regions: Inferences on the relative importance of slab pull and rift push in arc–back arc systems, *Tectonics*, 21(2), 1008, doi:10.1029/2001TC900026.

Hunziker, J. C., J. Desmons, and A. J. Hurford (1992), Thirty-two years of geochronological work in the central and western Alps: A review on seven maps, *Mem. Geol.*, 13, 60 pp.

Jiménez-Munt, I., M. Fernàndez, M. Torne, and P. Bird (2001), The transition from linear to diffuse plate boundary in the Azores-Gibraltar region: Results from a thin sheet model, *Earth Planet. Sci. Lett.*, 192, 175–189.

Jiménez-Munt, I., R. Sabadini, A. Gardi, and G. Bianco (2003), Active deformation in the Mediterranean from Gibraltar to Anatolia inferred from numerical modeling and geodetic and seismological data, *J. Geophys. Res.*, 108(B1), 2006, doi:10.1029/2001JB001544.

Jiménez-Munt, I., D. Garcia-Castellanos, and M. Fernàndez (2005), Thin-sheet modelling of lithospheric deformation and surface mass transport, *Tectonophysics*, in press.

Kastrup, U., M. L. Zoback, N. Deichmann, K. F. Evans, D. Giardini, and A. J. Michael (2004), Stress field variations in the Swiss Alps and the northern Alpine foreland derived from inversion of fault plane solutions, *J. Geophys. Res.*, 109, B01402, doi:10.1029/2003JB002550.

Kuhlemann, J., W. Frisch, I. Dunkl, and B. Székely (2001), Quantifying tectonic versus erosive denudation by the sediment budget: The Miocene core complexes of the Alps, *Tectonophysics*, 330, 1–23.

Laubscher, H. P. (1991), The arc of the western Alps today, *Eclogae Geol. Helv.*, 84, 631–659.

Lynch, H. D., and P. Morgan (1987), The tensile strength of the lithosphere and the localization of extension, in Continental Extension Tectonics,

edited by M. P. Coward, J. F. Dewey, and P. L. Hancock, *Geol. Soc. Spec. Publ.*, 28, 53–65.

Marotta, A. M., U. Bayer, M. Scheck, and H. Thybo (2001), The stress field bellow the NE German Basin: Effects induced by the Alpine collision, *Geophys. J. Int.*, 144, F8–F12.

Menard, G., P. Molnar, and J. P. Platt (1991), Budget of crustal shortening and subduction of continental crust in the Alps, *Tectonics*, 10, 231–244.

Neil, E., and G. Houseman (1997), Geodynamics of the Tarim Basin and the Tian Shan in central Asia, *Tectonics*, 16, 571–584.

Okaya, N., S. Cloetingh, and St. Mueller (1996), A lithospheric cross-section through the Swiss Alps-II. Constraints on the mechanical structure of a continent-continent collision zone, *Geophys. J. Int.*, 127, 399–414.

Pfiffner, O. A., S. Ellis, and C. Beaumont (2000), Collision tectonics in the Swiss Alps: Insight from geodynamic modeling, *Tectonics*, 19, 1065–1094.

Platt, J. P. (1986), Dynamics of orogenic wedges and the uplift of high-pressure metamorphic rocks, *Geol. Soc. Am. Bull.*, 97, 1037–1053.

Platt, J. P., J. H. Behrmann, P. C. Cunningham, J. F. Dewey, M. Helman, M. Parish, M. G. Shepley, S. Wallis, and P. J. Weston (1989), Kinematics of the Alpine arc and the motion history of Adria, *Nature*, 337, 158–161.

Ratschbacher, L., O. Merle, P. Davy, and P. Cobbold (1991), Lateral extrusion in the eastern Alps: 1. Boundary conditions and experiments scaled for gravity, *Tectonics*, 10, 245–256.

Regenauer-Lieb, K., and J.-P. Petit (1997), Cutting of the European continental lithosphere: Plasticity theory applied to the present Alpine collision, *J. Geophys. Res.*, 102, 7731–7746.

Ricou, L. E., and A. W. B. Siddans (1986), Collision tectonics in the western Alps, *Collision Tectonics*, edited by M. P. Coward and A. C. Ries, *Geol. Soc. Spec. Publ.*, 19, 229–244.

Rutter, E. H., J. Khazanehdari, K. H. Brodie, D. J. Blundell, and J. Waltham (1999), Synthetic seismic reflection profile through the Ivre Zone: Serie dei Laghi continental crustal section, northwestern Italy, *Geology*, 27, 79–82.

Schlunegger, F., and S. D. Willett (1999), Spatial and temporal variations in exhumation of the central Swiss Alps and implications for exhumation mechanisms, in *Exhumation Processes: Normal Faulting, Ductile Flow, and Erosion*, edited by M. Brandon and S. D. Willett, *Geol. Soc. Spec. Publ.*, 154, 157–180.

Schmid, A. M., O. A. Pfiffner, N. Froitzheim, and G. Schonborn (1996), Geophysical-geological transect and tectonic evolution of the Swiss-Italian Alps, *Tectonics*, 15, 1036–1064.

Sperner, B., L. Ratschbacher, and M. Nemčok (2002), Interplay between subduction retreat and lateral extrusion: Tectonics of the western Carpathians, *Tectonics*, 21(6), 1051, doi:10.1029/2001TC901028.

Sobouti, F., and J. Arkani-Hamed (1996), Numerical modelling of the deformation of the Iranian plateau, *Geophys. J. Int.*, 126, 805–818.

Stewart, J., and A. B. Watts (1997), Gravity anomalies and spatial variations of flexural rigidity at mountain ranges, *J. Geophys. Res.*, 102, 5327–5352.

Vialon, P., P. Rochette, and G. Menard (1989), Indentation and rotation in the western Alpine arc, in *Alpine Tectonics*, edited by M. P. Coward, D. Dietrich, and R. G. Park, *Geol. Soc. Spec. Publ.*, 45, 329–338.

Waldhauser, F., R. Lippitsch, E. Kissling, and J. Ansorge (2002), High-resolution teleseismic tomography of upper-mantle structure using an a priori three-dimensional crustal model, *Geophys. J. Int.*, 150, 403–414.

Watts, A. B. (1992), The effective elastic thickness of the lithosphere and the evolution of foreland basins, *Basin Res.*, 4, 169–178.

Watts, A. B., and E. B. Burov (2003), Lithospheric strength and its relationship to the elastic and seismogenic layer thickness, *Earth Planet. Sci. Lett.*, 213, 113–131.

Watts, A. B., and J. Stewart (1998), Gravity anomalies and segmentation of the continental margin offshore West Africa, *Earth Planet. Sci. Lett.*, 156, 239–252.

Wortmann, U. G., H. Weissart, H. Funk, and J. Hauck (2001), Alpine plate kinematics revisited: The Adria problem, *Tectonics*, 20, 134–147.

D. Garcia-Castellanos and I. Jiménez-Munt, Institute of Earth Sciences "Jaume Almera," CSIC, Lluís Solé i Sabarís s/n, E-08028 Barcelona, Spain. (danielgc@ija.csic.es; ivone@ija.csic.es)

A. M. Negredo, Department of Geophysics, Faculty of Physics, Universidad Complutense de Madrid, E-28040 Madrid, Spain. (anegredo@fis.ucm.es)

J. P. Platt, Department of Earth Sciences, University of Southern California, Los Angeles, CA 90089-0740, USA. (jplatt@usc.edu)

Figure 4.   Model results at the last stage (35 Myr, corresponding to the present) for (left) model A, temperature-dependent viscosity and constant effective strain rate of 4×10^{-16} s^{-1} thorough the entire model domain; (middle) model B, temperature- and strain rate-dependent viscosity; and (right) model C, same as model B but incorporating erosion and sedimentation, $K_d = 1000$ m^2 yr^{-1}. (a–c) Actual topography in the study area (color shading) and the model-predicted topography (contours). (d–f) Predicted Moho depth and (g–i) lithospheric mantle thickness (vertical distance between the 1300°C isotherm and the Moho). (j) Amount of erosion/sedimentation predicted in model C (negative values for erosion and positive for sedimentation). The coastline of the study area is plotted for reference. Note that the three models incorporate the same boundary conditions and therefore the same amount of mass input and total lithospheric shortening. Differences in topography and thickness distributions are due exclusively to the different rheology assumed (compare models A and B) and to the effects of surface transport (compare models B and C).
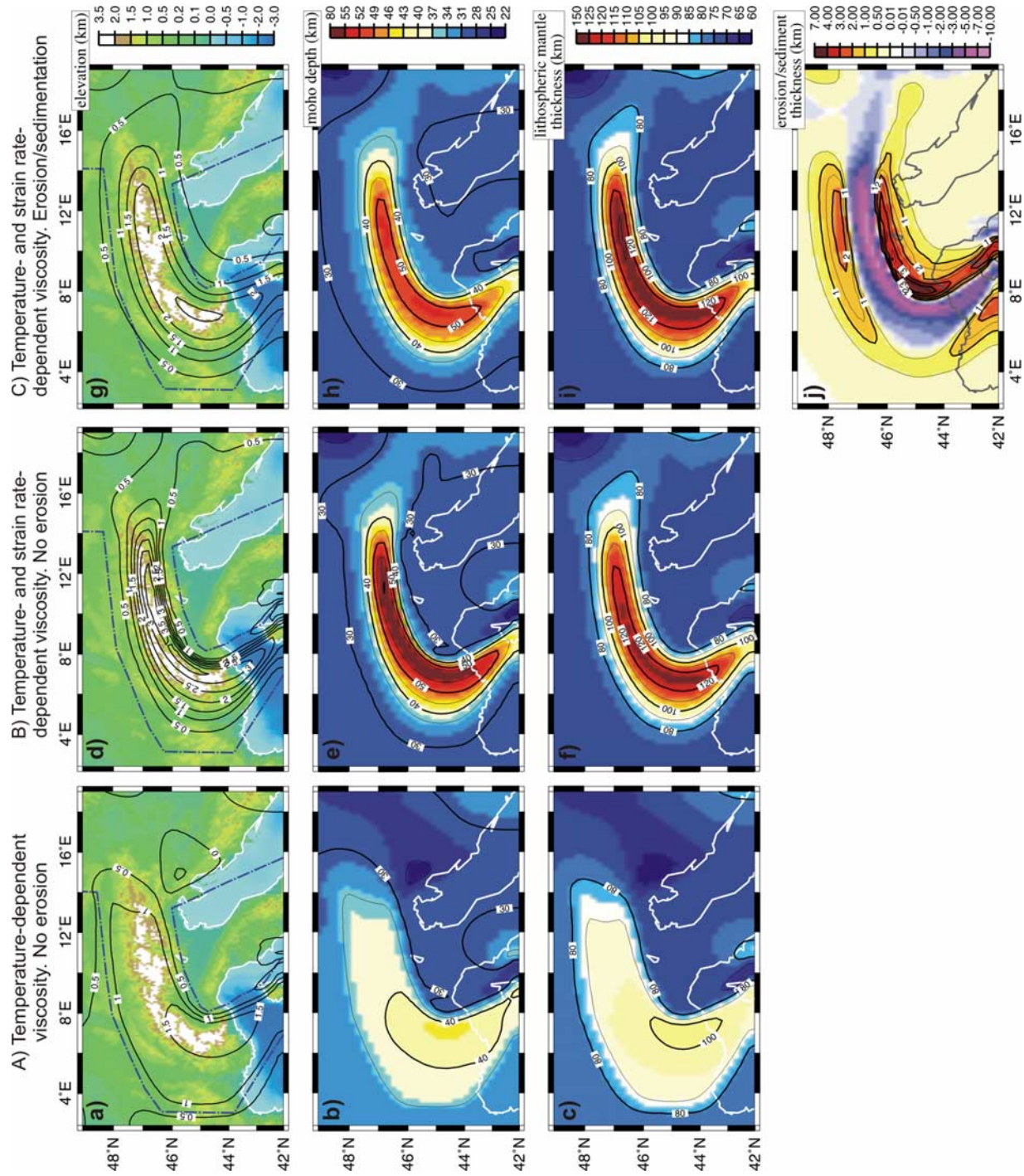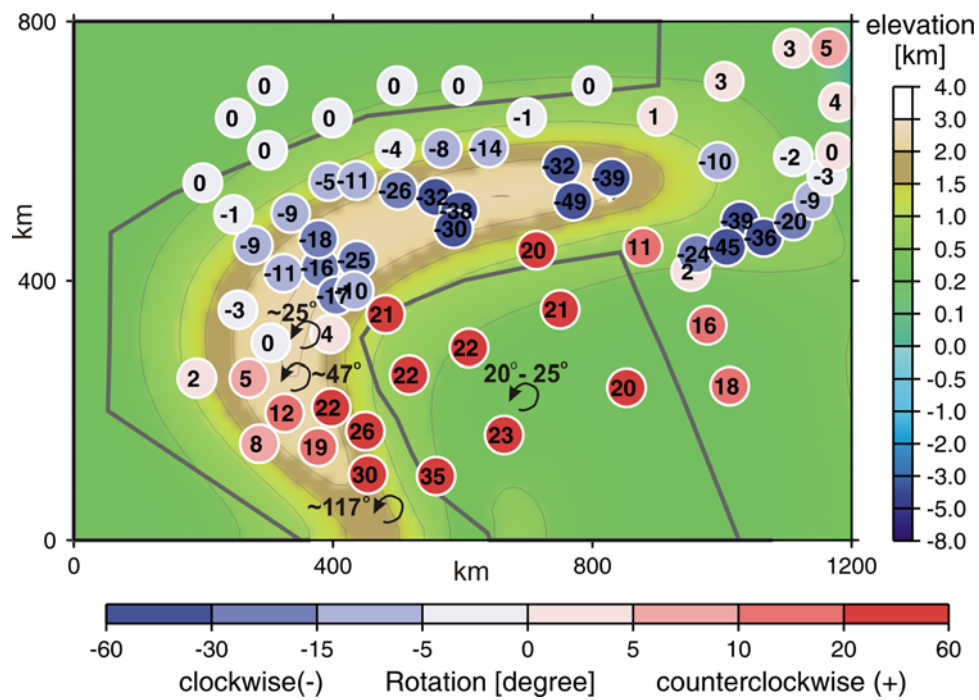
Figure 4

Figure 7. Vertical axis rotations predicted by the model C since 35 Ma (color circles). These are compared with paleomagnetic measurements for the western Alps since the Oligocene (black arrows and numbers [*Collombet et al.*, 2002]). Blue and red indicate clockwise and counterclockwise rotation, respectively.